ISSN 1067-8212, Russian Journal of Non-Ferrous Metals, 2017, Vol. 58, No. 2, pp. 168–173. © Allerton Press, Inc., 2017.

NANOSTRUCTURED MATERIALS AND FUNCTIONAL COATINGS

Preparation of Nanosized Zinc Oxide by Vacuum Oxidation and Kinetic Study of Oxidation[1]

Rong Liang Zhang*, Li Lei Ji, Yang Zhang, Ai Dong Huang, and Ai Bo Shi

School of Metallurgical and Materials Engineering, Jiangsu University of Science and Technology, Jiangsu, Zhangjiagang 215600, China

**e-mail: zhangrljx19201@163.com*

Received July 13, 2016

Abstract—Nanosized zinc oxide was prepared with a vacuum oxidation method by using hot-dip galvanizing slag as the raw material and air as the oxygen source. The oxidation kinetics curves of zinc vapor at different pressures were plotted by thermogravimetry, and the morphology of ZnO was observed by scanning electron microscopy. The nanosized ZnO products were hexagonal wurtzite crystals with the purity ≥99.98. When parabolic kinetics occurred, the ZnO products were granular, amorphous, tetra-needle-like or single needle-like. In the case of linear kinetics, the products were short tetra-needle-like or needle-like crystals. Zinc oxidation was controlled by the contracting spherical model R_3 initially and the three-dimensional diffusion model D_4 thereafter, with the apparent activation energies of 101.3–122.1 kJ/mol and 111.2–143.4 kJ/mol respectively.

Keywords: vacuum, nanosized zinc oxide, kinetics, morphology

DOI: 10.3103/S1067821217020134

1. INTRODUCTION

Nanosized zinc oxide, which has small particle size, large surface area, surface effect and quantum size effect, excels ordinary ones in non-toxicity, fluorescence, piezoelectricity, as well as capability to absorb and to scatter UV light. Therefore, it has been widely applied in the fields of rubber, ceramics, household chemicals, coatings and magnetic materials, etc., and it has been employed to prepare gas sensors, fluorescent materials, UV-shielding materials, rheostats, image-recording materials, pressure-sensitive materials, piezoelectric materials and efficient catalysts, etc. [1–12].

Currently, nanosized ZnO is prepared with high-purity zinc salts or metal zinc. Instead, using the abundant hot-dip galvanizing slag can reduce the cost of production. Hot-dip galvanizing slag contains over 90% Zn and impurities such as Fe in majority and small amounts of Al, Sn, Pb, Cd, Cu and Ni. Under vacuum, the impurities, except for a small amount of Cd, are volatilized at lower than 1273 K, so metal zinc is the main product. Han et al. managed to extract metal zinc from hot-dip galvanizing slag by vacuum distillation [13], based on which we aimed to directly prepare nanosized ZnO with the same raw material by vacuum oxidation.

Recently, amorphous, granular, single needle-like, tetra-needle-like and multi-needle-like zinc oxides have been prepared from zinc vapor under various oxidative conditions [14–19]. To clarify the mechanism for different morphologies, it is of great significance to study the oxidation behaviors of zinc vapor under different conditions, and to associate macroscopic morphology with the microscopic reaction of crystal growth. Since it remains difficult to continuously measure the changes of weight gain rate with currently available vacuum equipments, kinetics studies on nano-oxides under vacuum conditions have never been reported hitherto. At a given total pressure, inert gases can, as reduction of the total pressure does, decrease the partial pressure of reactants. Therefore, when the total pressure is fixed, vacuum conditions can be simulated by mixing inert gas N_2 and O_2 at different volume ratios to alter the reactant (O_2) partial pressure.

To this end, the aim of this study was to synthesize nanosized ZnO with vacuum oxidation by using hot-dip galvanizing slag as the raw material and air as the oxygen source. The system pressure was adjusted by changing the ratio of N_2 to O_2, at which kinetics of zinc vapor oxidation was studied by thermogravimetry (TGA) and corresponding curves were plotted. Besides, the morphology of ZnO was observed by scanning electron microscopy (SEM) to postulate the reaction mechanism by exploring the relationship between product morphology and changes of oxidation kinetics, and to determine kinetic parameters.

[1] The article is published in the original.

Table 1. Chemical constitution of hot-dip galvanizing slag (mass fraction), %

Constitutions	Zn	Ni	Fe	Cd	Mn	Cu	Pb	Al	Sn
Content	95.20	0.024	4.70	0.0003	0.0072	0.0038	<0.005	0.038	<0.001

2. EXPERIMENTAL

2.1. Materials and Apparatus

Hot-dip galvanizing slag was provided by Changshu Fengfan Power Equipment Co., Ltd., with its chemical constitution listed in Table 1.

High-purity N_2 and O_2 were mixed at different volume ratios. The pressures of (4.97% O_2 + 95.03% N_2), (4.55% O_2 + 95.45% N_2) and (4.14% O_2 + 95.86% N_2) equal 23975 Pa, 21975 Pa and 19975 Pa respectively.

TGA experiment was performed on a TGA/DSC1 thermoanalyzer (Mettler, Switzerland). Morphology was observed and particle size was measured by JSM-7001F thermal field emission scanning electron microscope (JEOL, Ltd., Japan). Crystal structure was analyzed by Shimadzu XRD-6000 X-ray diffractometer.

Impurity contents were determined by inductively coupled plasma atomic emission spectroscope (IRIS Advantage) and atomic absorption spectrometer (SpectrAA 220FS).

2.2. Methods

About 80 mg sample was put into a corundum crucible and adjusted to the same height by gentle knocking. Then the crucible was put in the TGA/DSC1 thermoanalyzer that was heated and added a mixture of N_2 and O_2 at the flow rate of 50 mL/min, and the temperature was kept constant for 50 min. To eliminate the influence of sample amount on TG curves, the rate of zinc's oxidation into ZnO was expressed as α, and can be determined by the related weight gain rate within the reaction time.

3. RESULTS AND DISCUSSION

3.1. Oxidation of Zinc and Characterizations of Product

Figure 1 shows the α-t curves of zinc vapor under different conditions, and Fig. 2 shows the corresponding SEM images.

At the beginning of reaction, the oxidation rate of zinc vapor increased with rising system pressure at all

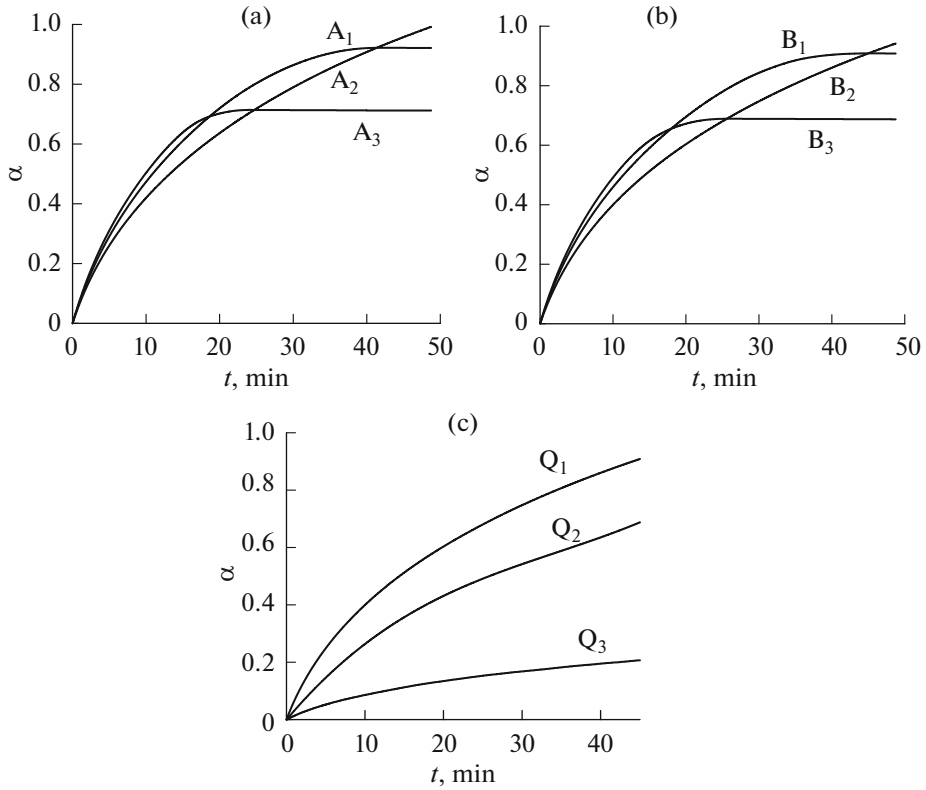

Fig. 1. Relationships between the rate of zinc's oxidation into ZnO and the reaction time of zinc vapor under different conditions. (1—900, 2—850, 3—800°C; A—23975, B—21975, Q—19975 Pa).

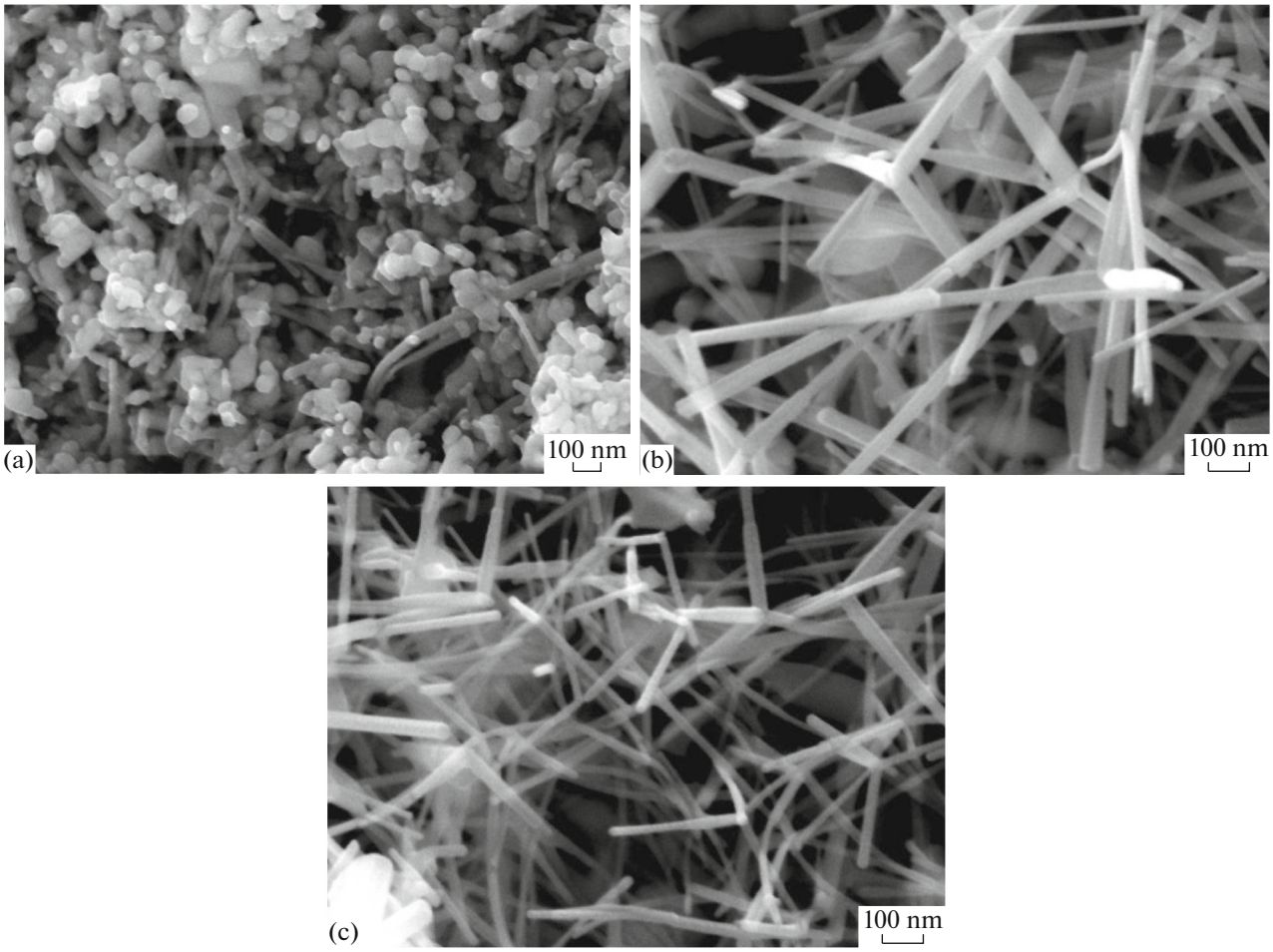

Fig. 2. SEM images of ZnO. ((a), (b), and (c) are particles obtained in A, B, and Q modes respectively).

tested temperatures and reached over 0.9 maximally with extended time. At the same temperature, curves A, B and Q presented different tendencies, and the former two followed parabolic kinetics as the characteristic of common gas-solid reactions. The products corresponding to curve A were mainly granular or amorphous (Fig. 2a), and those corresponding to curve B were mostly tetra-needle-like or single needle-like (Fig. 2b).

As the reaction progressed, α values of curves A_2 and B_2 exceeded those of curves A_1 and B_1 for the first time (Figs. 1a, 1b), which can be attributed to the escape of high-pressure zinc vapor from the reactor because dense oxide layers on the molten metal surface ruptured at 900°C. In contrast, the oxide layers moderately ruptured in the presence of zinc vapor at 850°C, but α still gradually increased because the unoxidized metal zinc underwent oxidation. Hence, high temperature was not necessarily conducive to the preparation of nanosized ZnO during vacuum oxidation. For curves A_3 and B_3, the vapor pressure of metal zinc barely affected the dense oxide layers at 800°C, so α was only 0.7 owing to the coating of most zinc. The above presumption was verified by puncturing the oxide layers at the end of reaction.

As shown in Fig. 1c, α keeps increasing with elapsed reaction time. At the beginning of reaction, α and t were linearly related due to rapid oxidation. Subsequently, the reaction decelerated at a certain oxidation rate, which can be ascribed to the formation of dense oxide layers that retarded considerable evaporation of metal zinc as well as the lack of oxygen in reaction system for further zinc oxidation. Most products were short tetra-needle-like or single needle-like crystals (Fig. 2c), with their XRD results shown in Fig. 3.

As evidenced by the sole sharp, intense diffraction peak of ZnO, the products were highly pure as integral, hexagonal wurtzite crystals without impurity phases. Besides, Table 2 shows that the purity of ZnO is not lower than 99.98%.

3.2. Postulation of Reaction Mechanism

As exhibited in Fig. 1c, α and t are linearly related when the partial pressures of zinc vapor and oxygen

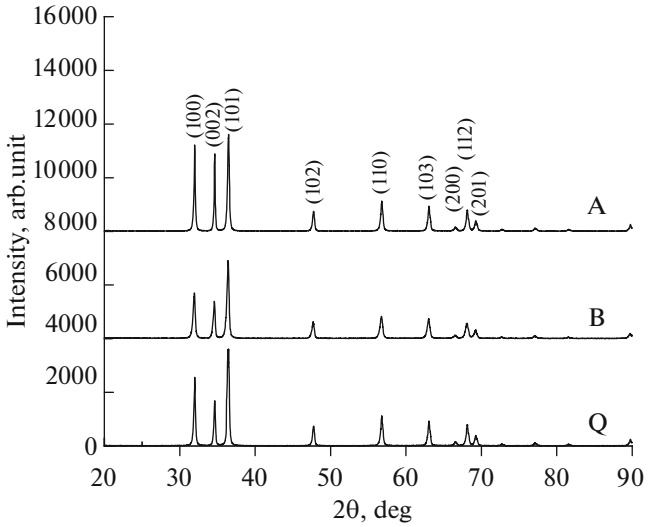

Fig. 3. XRD results of ZnO prepared under different conditions.

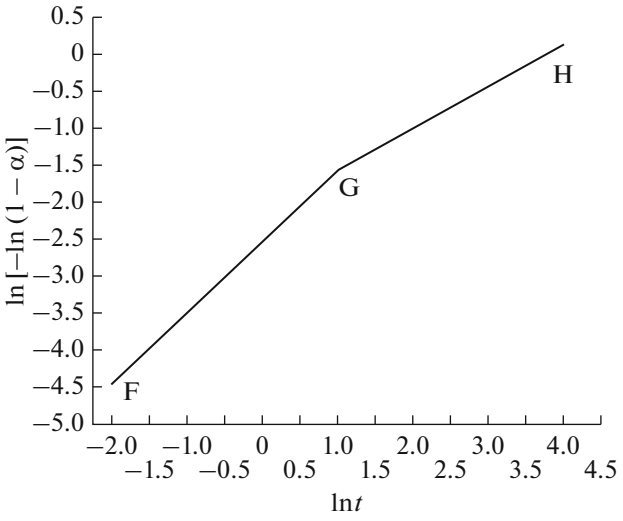

Fig. 4. Relationships between ln[–ln(1 – α)] and ln*t*.

remain unchanged, during which the evaporation rate of metal zinc predominantly controls the reaction rate. On the contrary, curves A and B changed more complicatedly

Taking the data at 900°C as the example, the data points of curve Ai could not be fitted by a straight line with the double logarithmic In In method (Fig. 4), suggesting that zinc vapor may be oxidized following different kinetics sequentially. The slopes of line segments FG and GH were calculated as 1.07 and 0.57 respectively by linear regression. Accordingly, the reaction corresponding to segment FG, as referenced by known slopes [20], was controlled by the contracting spherical model R_3. On this basis, the reaction corresponding to segment GH was governed by the three-dimensional diffusion model D_4 other than the two-dimensional diffusion model D_2.

Similarly, other curves A and B all suggested that the oxidation of metal zinc was first controlled by model R_3 and thereafter by model D_4.

3.3. Calculation of Kinetics Parameters for Oxidation

Figure 4 gives the transition time of reaction kinetics. The differential kinetic equations for the contracting spherical model R_3 and the three-dimensional diffusion model D_4 are expressed below.

$$\begin{cases} \dfrac{d\alpha}{dt} = 3k_1(1-\alpha)^{2/3} & (R_3) \\ \dfrac{d\alpha}{dt} = \dfrac{3}{2}k[(1-\alpha)^{1/3} - 1]^{-1}. & (D_4) \end{cases} \quad (1)$$

Integration of Eq. (1) gives:

$$\begin{cases} 1-(1-\alpha)^{1/3} = k_1 t & (R_3) \\ 1 - 2\alpha/3 - (1-\alpha)^{2/3} = kt. & (D_4) \end{cases} \quad (2)$$

Reaction rate constants in the early stage of oxidation, i.e. k_1 and k_2, were derived (Table 3) from the slopes of lines describing the relationship between $1-(1-\alpha)^{1/3}$ and t or between $1 - 2\alpha/3 - (1-\alpha)^{2/3}$ and t.

$$k = Ae^{-E/RT}. \quad (3)$$

Taking the logarithms of both sides of Eq. (3) gives:

$$\ln k = -E/RT + \ln A. \quad (4)$$

A straight line was plotted for $\ln k - 1/T$, from the slope and intercept of which activation energy E and frequency factor A were calculated (Table 4).

Table 2. Contents of impurities in products (mass fraction), %

Compositions	Ni	Fe	Cd	Mn	Cu	Pb	Al	Sn
Content	<0.003	0.0031	0.0004	<0.001	<0.001	<0.003	<0.001	<0.001

Table 3. Reaction rate constants

Temperature	800°C			850°C			900°C		
Pressure, Pa	19975	21975	23975	19975	21975	23975	19975	21975	23975
$k_1/10^{-3}$	19.5	24.1	28.7	29.9	34.6	45.6	62.5	80.1	96.3
$k_2/10^{-3}$	1.84	2.28	2.93	3.03	3.61	4.47	6.29	8.23	9.70

Table 4. Kinetics parameters under different conditions

Pressure	R_3 stage		D_4 stage	
	E_1, J mol^{-1} K^{-1}	A_1	E_2, J mol^{-1} K^{-1}	A_2
19975 Pa	101.3	2689.2	111.2	2807.3
21975 Pa	113.5	3877.2	126.6	4464.2
23975 Pa	122.1	6328.2	143.4	7556.3

4. CONCLUSIONS

(1) Structurally integral hexagonal wurtzite ZnO nanocrystals with the purity >99.98 were prepared with a vacuum oxidation method based on hot-dip galvanizing slag by using air as the oxygen source.

(2) When the reaction followed the parabolic kinetics, the ZnO products were granular, amorphous, tetra-needle-like or single needle-like. In the case of linear kinetics, however, short tetra-needle-like or needle-like ZnO crystals were obtained.

(3) Zinc oxidation was sequentially controlled by the contracting spherical model R_3 and the three-dimensional diffusion model D_4, with the apparent activation energies of 101.3–122.1 kJ/mol and 111.2–143.4 kJ/mol respectively.

ACKNOWLEDGMENTS

This work was financially supported by the National Natural Science Foundation of China (51304082), and the Natural Science Foundation of Jiangsu province (no. BK2009574).

REFERENCES

1. Mahuya, C., Jana, D., and Sanyal, D., Positron annihilation characterization of nanocrystalline ZnO, *Vacuum*, 2013, vol. 87, pp. 16–20.
2. Chen, W.L., Yin, J., Huang, C.S., Wang, X.W., Yun, Z.H., and Bie, L.J., Preparation of formaldehyde gas sensing properties of gold nanoparticle modified ZnO nanorods array, *Chin. J. Inorg. Chem. (Chin.)*, 2010, vol. 26, pp. 586–590.
3. Liu, C.S., Wang, L., Li, Z.W., Xu, Z., and Huang, J.H., Effect of hydrofluoric acid on morphology and wettability of micro-nano ZnO powders, *Chin. J. Nonferrous Met. (in Chin.)*, 2007, vol. 17, pp. 1690–1694.
4. Li, B., Liu, S.Q., Liu, L., Cui, Y.M., Guo, X.F., and Zhou, X.F., Fabrication of ZnO nanosheets based carambola-like microspheres and gas sensor properties, *Chin. J. Inorg. Chem. (Chin.)*, 2010, vol. 26, pp. 591–595.
5. Park, H., Tong, F., Sujan, A., Chung, Y., Park, M., and Tatarchuk, B.J., Growth of nanostructured ZnO on wearable fabrics for functional garment, *Mater. Lett.*, 2014, vol. 118, pp. 47–50.
6. Abbasi, M.A., Khan, Y., Hussain, S., Nur, O., and Willander, M., Anions effect on the low temperature growth of ZnO nanostructures, *Vacuum*, 2012, vol. 86, pp. 1998–2001.
7. Sangari, N.U. and Devi, S.C.J., Synthesis and characterization of nano ZnO rods via microwave assisted chemical precipitation method, *J. Solid State Chem.*, 2013, vol. 197, pp. 483–488.
8. Zhang, H.D., Long, Y.Z., Li, Z.J., and Sun, B., Fabrication of comb-like ZnO nanostructures for room-temperature CO gas sensing application, *Vacuum*, 2014, vol. 101, pp. 113–117.
9. Amirkhanlou, S., Ketabchi, M., and Parvin, N., Nanocrystalline/nanoparticle ZnO synthesized by high energy ball milling process, *Mater. Lett.*, 2012, vol. 86, pp. 122–124.
10. Zhao, C.L., Huang, Y., and Abiade, J.T., Ferromagnetic ZnO nanoparticles prepared by pulsed laser deposition in liquid, *Mater. Lett.*, 2012, vol. 85, pp. 164–167.
11. Nagajyothi, P.C., Minh An, T.N., Sreekanth, T.V.M., Lee, J.I., Lee, D.J., and Lee, K.D., Green route biosynthesis: Characterization and catalytic activity of

ZnO nanoparticles, *Mater. Lett.*, 2013, vol. 108, pp. 160–163.

12. Venkatesh, P.S. and Jeganathan, K.J., Investigations on the growth and characterization of vertically aligned zinc oxide nanowires by radio frequency magnetron-sputtering, *Solid State Chem.*, 2013, vol. 200, pp. 84–89.
13. Hang, L., Yang, B., Yang, B.Z., Dai, Y.N., Liu, D.C., and Xu, B.Q., Znic recovering from hot galvanized scraps by vacuum distillation, *Chin. J. Vacuum Sci. Technol. (Chin.)*, 2009, vol. 29, pp. 101–104.
14. Zhu, Y.W., Zhang, H.Z., Sun, X.C., Feng, S.Q., Xu, J., Zhao, Q., Xiang, B., Wang, R.M., and Yu, D.P., Efficient field emission from ZnO nanoneedle arrays, *Appl. Phys. Lett.*, 2003, vol. 83, pp. 144–146.
15. Zhang, R.L., Shi, A.B., and Jin, Y.X., and Hu, J., Preparation of nanosized zinc oxide by vacuum oxidation and behaviors of impurity elements, *Russ. J. Non-Ferrous Met.*, 2015, vol. 56, pp. 114–118.
16. Ko, Y.H. and Yu, J.S.J., Structural and antireflective properties of ZnO nanorods synthesized using the sputtered ZnO seed layer for solar cell applications, *J. Nanosci. Nanotechnol.*, 2010, vol. 10, pp. 8095–8101.
17. Leung, Y.H., Djurisic, A.B., Choy, W.C.H., Xie, M.H., Gao, J., Cheah, K.W., Man, K.Y.K., and Chan, W.K., Synthesis and properties of ZnO multipod structures, *J. Cryst. Growth*, 2005, vol. 274, pp. 430–437.
18. Park, J., Choi, H., Siebein, K., and Singh, R.K., Two-step evaporation process for formation of aligned zinc oxide nanowires, *J. Cryst. Growth*, 2003, vol. 258, pp. 342–348.
19. Hu, J.Q., Li, Q., Wong, N.B., Lee, C.S., and Lee, S.T., Synthesis of uniform hexagonal prismatic ZnO whiskers, *Chem. Mater.*, 2002, vol. 14, pp. 1216–1219.
20. Hu, R.Z. and Shi, Q.Z., *Kinetics of Thermal Analysis (Chin.)*, Beijing: Science Press, 2008.